Journal of Molecular Catalysis A: Chemical 318 (2010) 60–67

Contents lists available at ScienceDirect

Journal of Molecular Catalysis A: Chemical

journal homepage: www.elsevier.com/locate/molcata

Synthesis and characterization of Fe/CeO_2 catalysts: Epoxidation of cyclohexene

A. Satyanarayana Reddy[a], Chien-Yen Chen[a,*], Chien-Cheng Chen[b], Shu-Hua Chien[c], Chin-Jung Lin[c], Kao-Hung Lin[d], Chih-Lei Chen[e], Shiuan-Chih Chang[a]

[a] Department of Earth and Environmental Sciences, National Chung Cheng University, 168 University Road, Minhsiung, Chiayi 621, Taiwan
[b] Department of Biotechnology, National Kaohsiung Normal University, No. 62, Shenjhong Rd., Yanchao Township, Kaohsiung County 82444, Taiwan
[c] Institute of Chemistry, Academia Sinica, 128 Academia Road, Section 2, Nankang, Taipei 11529, Taiwan
[d] Sustainable Environment Research Center, National Cheng Kung University, Tainan 701, Taiwan
[e] Large Size OLED Technology Department, AU Optronics Corporation, No. 1 Li-Hsin Rd. 2, Hsinchu Science Park, Hsinchun 30078, Taiwan

ARTICLE INFO

Article history:
Received 6 May 2009
Received in revised form
12 November 2009
Accepted 13 November 2009
Available online 14 December 2009

Keywords:
Iron–cerium oxide
Cyclohexene oxidation
Catalyst

ABSTRACT

Oxidation of cyclohexene using aqueous hydrogen peroxide (30%, v/v) over iron–cerium oxide (x%Fe/CeO_2; x = 0, 2, 5, 10 and 20 mol%) prepared by co-precipitation was conducted in this study in order to assess the performance of the catalysts of varying composition, and catalytic activity and product selectivity were found to strongly depend on catalyst composition, acidity and reducibility. The effects of varying the catalyst composition, reaction temperature and solvent were investigated. Cyclohexene epoxide and 1,2-cyclohexanediol were found to be the main reaction products, along with small amounts of other oxygenated products. A high cyclohexene conversion rate of 99 mol% and an epoxide selectivity of 98 mol% were observed over 5%Fe/CeO_2 at 100 °C. The catalysts were characterized using various techniques and measures, including BET surface area, XRD, DRS UV–vis, potentiometric titration for acidity measurement, and XPS. XRD showed the formation of iron–cerium oxide solid solutions with cerianite cubic structures for all catalysts except FC4, and the DRS UV–vis results further indicated the formation of solid solutions. Analysis of Raman spectra revealed the presence of aggregate iron oxide species in case of 20%Fe/CeO_2 catalyst. TPR revealed enhancement of the reducibility of the ceria upon Fe doping, and the potentiometric titration results showed an increase in the number of acidic sites with increasing iron content up to 5% and a decrease thereafter. TPR and XPS analyses revealed the presence of highly dispersed Fe species in the 2%Fe/CeO_2 and 5%Fe/CeO_2 samples, whereas for the 10%Fe/CeO_2 and 20%Fe/CeO_2 catalysts, aggregates of Fe species were observed. Catalytic activity was found to be correlated with the composition and acidic properties of the catalyst.

1. Introduction

Owing to its elevated oxygen storage capacity and redox properties, cerium dioxide is suited to and widely used as a support or active species in various industrial heterogeneous catalysts and automotive three-way converters (TWC) [1–3]. The lattice oxygen mobility, oxide ion conductivity and oxygen storage capacity (OSC) of cerium oxide can be augmented by the substitution of another metal ion for cerium, ceria-supported metal/metal oxide catalysts being more active by several orders of magnitude in a number of redox reactions [2,3]. The doping of metal ions into ceria results in much-improved properties, and several ceria-based systems have been the focus of investigative research in the past [4]. It has been shown that the lower valence ions in ceria influence the energetic properties of the material by lowering the activation energy for oxygen migration [5]. Gold metal-supported ceria catalysts have the potential for use in different catalytic reactions such as CO and hydrocarbon oxidation, the water gas shift reaction, NOx reduction by CO and hydrocarbons, etc. [6].

Iron oxide, in pure or mixed form, has long been regarded as an important catalyst. Potassium-promoted iron oxide in reduced form is used as the commercial catalyst for ammonia synthesis in the Haber process [7], and iron-based catalysts have been extensively studied in terms of their catalytic activity in reactions such as alkylation, NOx reduction, steam reforming of hydrocarbons, the water gas shift reaction, conversion of benzene to phenol using N_2O as the oxidant, and syngas production. [8]. Given the effects of trivalent ions and those of smaller size on the structure and properties of catalysts, there is considerable scientific interest in the introduction of M^{3+} (e.g., Fe^{3+}) ions into the ceria lattice [9]: this addition of trivalent transition metals (Fe, Mn, Ni, Cu, etc.) has been reported to enhance the interaction of CO_2 in O_2-releasing reactions at lower temperatures. CeO_2–MO_x (Fe, Mn, Ni and Cu) solid solutions with high melting points and high conductivities of O^{2-} are some of the

* Corresponding author. Tel.: +886 5 2720411x66220; fax: +886 5 2720807.
E-mail addresses: chienyen.chen@gmail.com, yen@eq.ccu.edu.tw (C.-Y. Chen).

1381-1169/$ – see front matter © 2009 Elsevier B.V. All rights reserved.
doi:10.1016/j.molcata.2009.11.008

most reactive ceramics known and are used as resistive-type O_2 sensors for exhaust gas from automobiles [10]. The catalytic activity of CeO_2–Fe_2O_3 in the synthesis of 3-pentanone from 1-propanol has been investigated [11], and this catalyst in the form of thin films of different Ce/Fe ratios has been tested for use as an alcohol sensor [12]. Alkali-promoted iron catalysts exhibit better activity for Fischer–Tropsch synthesis, with remarkable differences in the 1-alkene selectivity and carbon number distribution [13]. Recently, iron-based catalytic systems have been designed for use in the gas phase epoxidation of propylene, utilizing nitrous oxide as a selective oxidant [14].

Oxidation of cyclohexene was carried out in this study in order to evaluate the performance of iron–ceria catalysts of varying composition. The selective oxidation of cyclohexene into various oxygenated products (e.g., cyclohexanone, cyclohexene epoxide, and adipic acid) using heterogeneous catalysts with different oxidants such as oxygen, air and peroxides has been reported elsewhere [15]. Catalytic liquid-phase epoxidation of cyclohexene is a commercially important reaction used to produce cyclohexene oxide, which is an essential organic intermediate in the production of fine chemicals. The production of epoxides paves the way to the development of mild and green chemical processes for the synthesis of adipic acid, the raw material used in the production of nylon 66 [16]. The titanium- and cerium-containing mesoporous silicate materials Ti-MMM-2 and Ce-SBA-15 have been used to catalyze cyclohexene oxidation to adipic acid with aqueous hydrogen peroxide under solvent-free conditions [17]. A simple, green and efficient microwave approach to the selective oxidation of cyclohexane to different oxygenated products by adjusting the reaction conditions using a cobalt-salen-SBA-15 catalyst has also been reported [18], and the use of heterogeneous catalysts for cyclohexene oxidation has been demonstrated, with high selectivities of 2-cyclohexene-1-one [19,20], 2-cyclohexene-1-ol [19–22], cyclohexene oxide [23], trans-cyclohexane-1,2-diol [23], and di-(2-cyclohexenyl) ether [24,25]. The use of a clean oxidant such as H_2O_2, which produces water as the only by-product, is another important feature of a green chemical reaction [26,27].

In this work, iron-doped ceria catalysts were investigated in terms of their activity in catalyzing cyclohexene oxidation, the aim being to increase the oxygen storage capacity and oxygen mobility. Various iron–ceria catalysts were thoroughly investigated and physicochemically characterized using a number of techniques in order to understand the structure–activity relationship. Cyclohexene oxidation using H_2O_2 as the oxidant was used as the catalytic activity test reaction, and the effects of reaction temperature and solvent were also investigated.

2. Experimental

2.1. Catalyst preparation

A series of iron–ceria mixed oxide (x%Fe/CeO_2, x = 0, 2, 5, 10 and 20) catalysts was prepared by co-precipitation from aqueous solutions of $Fe(NO_3)_3{\cdot}9H_2O$ and $Ce(NO_3)_3{\cdot}xH_2O$ containing cetyltrimethyl ammonium bromide (CTAB) by the addition of KOH solution. Briefly, the catalysts were synthesized by the slow addition of KOH solution (0.25 M) to the mixtures of metal precursor solutions (0.1 M each) containing CTAB (above the CMC) in stoichiometric proportions in a 1-L round-bottom flask under vigorous stirring at room temperature. During the precipitation of the metal salts, the pH of the resultant mixture was maintained at 9; the final pH of the gel was then adjusted to 10, followed by aging the gel at room temperature overnight. The metal hydroxide thus obtained was filtered and washed thoroughly with Milli Q water until the pH of the filtrate attained ~7.5. The metal hydroxide precipitates were then dried at 120 °C for 12 h, followed by calcination at 550 °C in air for 6 h. The samples are designated herein as FC0, FC1, FC2, FC3 and FC4, for x = 0, 2, 5, 10 and 20 in x%Fe/CeO_2, where x denotes the fraction of iron taken for the preparation.

2.2. Catalyst characterization

Powder X-ray diffraction (XRD) analysis was conducted using a Shimadzu X-ray diffractometer (model LabX XRD-6000) equipped with Ni-filtered CuKα (λ = 0.1541 nm, 40 kV A, 30 mA) radiation and a graphite crystal monochromator. The data were collected in the 2θ range of 10–80° with a step size of 0.02° and a scan rate of 2° min^{-1}. The mean crystallite size of the samples was calculated using the Debye–Scherrer equation, using the FWHM value corresponding to the high intense peak at 29.1°, and the unit cell parameter 'a' was determined using PDP11 software.

The BET surface area (S_{BET}) of the samples was measured by nitrogen adsorption at 77 K on a Micromeritics surface area and porosity analyzer (ASPS-2020). The catalyst samples were evacuated at 573 K for 3 h before N_2 adsorption. Diffuse-reflectance UV–visible spectra were recorded on a Shimadzu UV-2550 spectrophotometer in the 200–800 nm range at room temperature. Laser Raman spectra were obtained on a DILOR XY spectrometer equipped with a liquid nitrogen-cooled CCD detector at ambient temperature and pressure. The emission line at 514.5 nm from the Ar^+ ion laser (Spectra Physics) was focused on the sample under a microscope; the power of the incident beam on the sample was 3 mW and the time of acquisition was adjusted according to the intensity of the Raman scattering.

Temperature-programmed reduction (TPR) profiles were obtained using a Micromeritics Autochem model 2910 instrument. The samples were pretreated in high-purity (99.98%) argon (20 ml/min) at 773 K for 3 h. After cooling to ambient temperature, the argon atmosphere was replaced by a 5% H_2 in argon mixture, and the catalyst was heated to 873 K at a rate of 5 K/min. The flow rate of the H_2–Ar mixture used for this purpose was 40 ml/min. The water produced during the reduction step was condensed and collected in a cold trap immersed in the slurry of an isopropanol–liquid nitrogen mixture. X-ray photoemission spectra (XPS) were acquired using a Shimadzu (ESCA 3400) spectrometer with a MgKα X-ray source ($h\nu$ = 1253.6 eV). Disks of fresh sample were scraped *in situ* prior to the recording of spectra. XPS analysis was performed at the ambient temperature and a pressure typically of the order of less than 10^{-6} Torr. Charging of catalyst samples was corrected by setting the binding energy of the adventitious carbon (C 1s) at 284.6 eV.

The acidity of the solid samples pre-heated at 200 °C was measured by the potentiometric titration method. 50 mg of catalyst suspended in acetonitrile (20 ml) was stirred for 3 h and the suspension was then titrated with a solution of n-butylamine (0.05 N) in acetonitrile at a flow rate of 0.05 ml/min. The variation in electrode potential was measured using an instrument with a digital pH meter and a standard calomel electrode. The acidity of the catalyst as measured using this technique enables the determination of the total number of acidic sites and their strength. In order to interpret the results, it has been suggested that the initial electrode potential (E in mV) be taken as the maximum acidic strength of the surface sites and that the range between that and where the plateau is reached (mequiv./g cat) can be considered the total number of acidic sites [28,29].

2.3. Catalytic activity measurements

The catalysts were evaluated in a batch reactor (Parr autoclave, 100 ml) equipped with a heating controller. The reaction was carried out at atmospheric pressure after flushing the reac-

Table 1
Textural properties of the iron–ceria catalysts.

Catalyst	Composition (molar ratio)		S_{BET}[a] (m^2/g)	a[b] (Å)	Crystallite size (Å)	Total acidity ($\times10^{-3}$ mequiv. amine/m^2)	Initial electrode potential (mV)
	Fe/Ce[c]	Fe/Ce[d]					
FC0	0/100	0/100	73	5.40	36	6.4	−88.0
FC1	0.26/17.34	0.20/16.2	83	5.37	36	21.9	+2.6
FC2	1.07/17.08	0.91/16.5	88	5.37	38	25.9	+33.8
FC3	2.68/16.56	2.40/16.0	90	5.36	41	13.4	−19.6
FC4	5.37/15.68	5.1/15.1	80	5.34	43	17.1	−10.8

[a] Surface area after calcination at 500 °C.
[b] Unit cell parameter.
[c] Composition in preparation gel.
[d] Composition in the final product.

tor with inert gas (N_2) and at a temperature of 100 and 120 °C using 0.1 g of catalyst. Before the reaction, the catalysts were activated in air at 120 °C, followed by cooling to room temperature. Weighed amounts of reactants were then fed into the reactor. After completion of the reaction (8 h), the reactor was cooled to room temperature, followed by the separation of the solid catalyst by centrifugation and subsequent product analysis. Analysis of the organic phase was carried out using a gas chromatograph (Clarus 500, PerkinElmer Instruments, USA) equipped with an Elite-5 capillary column (30 m, 0.32 mm i.d., 1 μm film thickness) and a FID. All of the products were identified using pure authentic (Aldrich) standards and GC–MS. The conversion rate of cyclohexene was calculated based on the fraction of cyclohexene reacted, whereas the selectivity was calculated from the percentage of the given product in the mixture. Aliquots of the solution were taken after the completion of the reaction course in order to determine the concentration of H_2O_2 by iodometric titration.

3. Results and discussion

3.1. Catalyst characterization

The physical properties of the freshly calcined samples are summarized in Table 1. The BET surface area of the catalysts increased initially with increasing iron content in the ceria up to 10 mol% (73–90 m^2/g), while a further increase in iron content (i.e., to 20% Fe) resulted in a smaller surface area (80 m^2/g). Incorporation of iron therefore initially enhanced the surface area of the samples. The average crystallite sizes D of the Fe–CeO_2 samples were calculated from the X-ray line broadening of the reflections of (1 1 1) using Scherrer's equation (i.e., $D = K\lambda/(\beta\cos\theta)$, where λ is the wavelength of the X-ray radiation, K is a constant taken as 0.9, θ is the diffraction angle, and β is the full width at half-maximum (fwhm)), and were found to be in the range 30–43 nm (Table 1). The crystallite sizes of the samples also increased with increasing iron content. The unit cell parameter 'a' for the cubic fluorite lattice and the unit cell volume decreased with iron incorporation. The XRD patterns of catalysts calcined at 500 °C are shown in Fig. 1. The sample without iron loading (FC0) exhibited the cubic fluorite structure of CeO_2 (cerianite), as identified using standard data (JCPDS file no. 34-0394). All the samples, even after the incorporation of iron, typically showed diffraction peaks corresponding to cerianite, and the cerianite structure did not undergo any changes after the incorporation of 2–20% of iron. Diffraction peaks corresponding to iron oxide species were observed only in the sample containing a high level of iron (FC4). The absence of iron oxide phases in the samples identified from the XRD results may indicate substitution of iron into the ceria fluorite lattice, resulting in the formation of a solid solution of iron–cerium oxide; however, the presence of finely dispersed iron oxide on the ceria cannot be ruled out, as it may not be detected by XRD. It was also observed that the crystalline nature of the samples increased after the incorporation of iron, indicating that the loading of iron improved the crystallinity. A clear shift in the high intense peak position of (1 1 1) towards higher 2θ values for FC4 was observed at ~29, as shown in the inset of Fig. 1. It was noted that the lattice parameter 'a' values for the calcined samples were lower than that reported for CeO_2 (a = 5.4113 Å) in the standard data, JCPDS 34-0394, whereas the value for the pure CeO_2 was close to that reported in the standard data.

The optical responses of the iron–ceria catalysts were investigated by UV–visible spectroscopy, and the results are presented in Fig. 2. The absorption edge of the samples extended to 500 nm for FC0 and FC2 and up to ~700 nm for FC1, FC3, and FC4. The UV–vis spectra showed distinctly higher absorptions in the UV and visible regions with increasing iron content. The band in the UV region arises due to charge transfer transitions from O 2p to Ce 4f bonds, which overrun the well-known f-to-f spin–orbit splitting of the Ce 4f state [30]. It was noted that the spectral intensity of the samples increased in the UV region with increasing Fe content, which

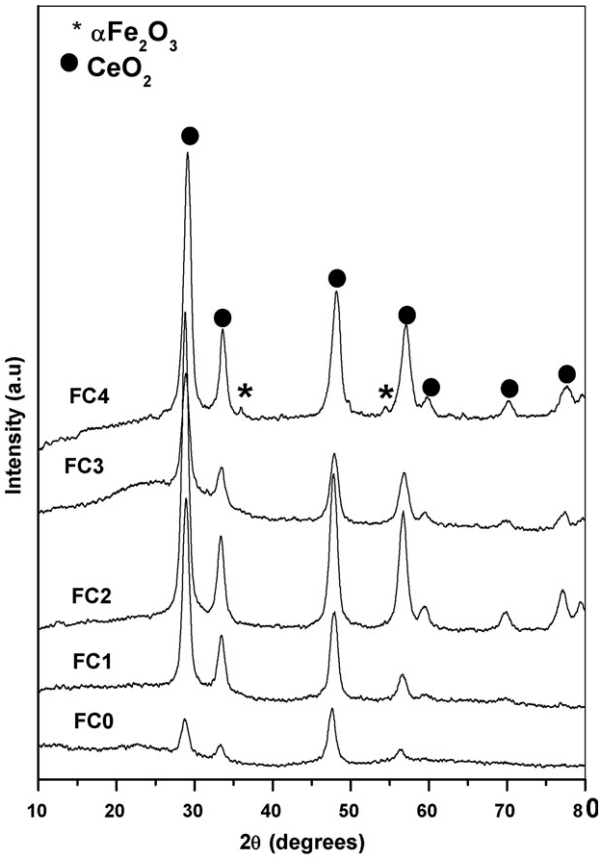

Fig. 1. X-ray diffraction of the fresh Fe–CeO_2 samples calcined at 500 °C. Inset: magnified portion of the high intense peak.

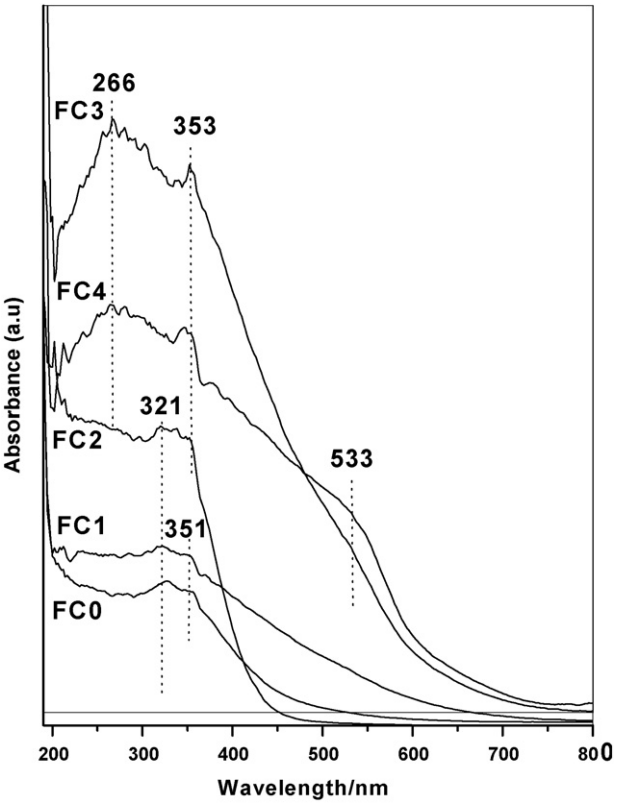

Fig. 2. UV–visible spectra of the fresh Fe–CeO_2 samples calcined at 500 °C.

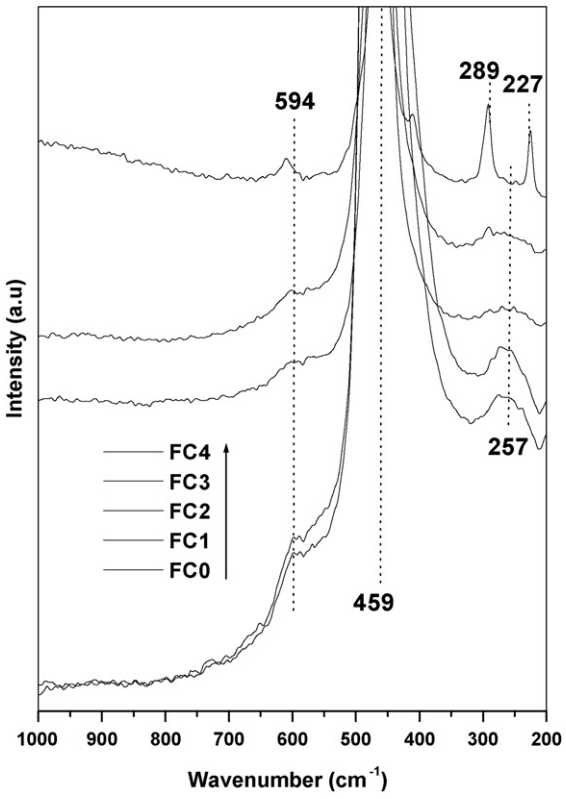

Fig. 3. Raman spectra of the Fe–CeO_2 samples calcined at 500 °C.

may be due to $O \rightarrow Fe^{3+}$ ligand-to-metal charge transitions (LMCT). Charge transfer occurs from the highest lying O 2p orbitals to the half-occupied Fe 3d orbitals ($t_{2g} \rightarrow e_g$ in O_h symmetry and $e \rightarrow t_2$ in T_d symmetry) [31]. Schwidder et al. reported that the band at <300 nm is that of isolated Fe^{3+}, the band at 300–400 nm is due to oligometric clusters, and the band at >400 nm to large α-Fe_2O_3 particles [32]; however, it is not possible to distinguish between isolated and binuclear Fe^{3+} species from UV–vis spectra, as a strong shift of LMCT bands is not expected [33]. On the other hand, the absorption in the visible region (>450 nm) may be due to *d–d* transitions in α-Fe_2O_3 [34–36]. The absorption band near 533 nm may be due to $^6A_{1g} \rightarrow {}^4T_{1g}$ and $^6A_{1g} \rightarrow {}^4T_{2g}$ transitions; however, the position of this band depends on the size of the α-Fe_2O_3 particles [32,33]. The Raman spectra of the iron–ceria samples are presented in Fig. 3. Pure ceria and the sample with a low iron content (FC1) exhibited main peaks at 257, 459 and 594 cm^{-1} due to the ceria phase, and these are ascribed to the doubly degenerate TO (transverse optical) mode, the triply degenerate Raman-active mode, and the non-degenerate LO (longitudinal optical) mode, respectively [37,38]. The intensity of the Raman peak at 257 cm^{-1} decreased with increasing iron content, which clearly indicates the occurrence of structural changes due to interaction with the iron species. The distinct new Raman bands observed for the FC4 sample at 227 and 289 cm^{-1} are due to Fe_2O_3 species [39]; in corroboration, diffraction peaks corresponding to Fe_2O_3 species were also observed for FC4. It is important to note that the peak assigned to ceria at 594 cm^{-1} shifted to a higher wave number (607 cm^{-1}) with increasing iron oxide content. As has been stated above, the XRD measurements also showed evidence of the formation of a solid solution when up to 20% iron was added into ceria. Therefore, this shift in the position of the peak (607 cm^{-1}) assigned to ceria in the Raman spectra of mixed oxides provides evidence of noticeable interaction between the constituent metal oxides.

The temperature-programmed reduction (TPR) technique was used to investigate the reducibility of the catalysts and determine the types of metal oxide species present in the various samples. The TPR profiles are presented in Fig. 4, from which it can be seen that the profile of pure ceria showed two reduction peaks at 601 and 670 °C, which can be attributed to the surface and bulk reduction of CeO_2 to Ce_2O_3, respectively [40,41]. The iron-incorporating ceria samples exhibited an increase in the reducibility of the ceria, resulting in a shift in the reduction peak to the lower temperature. No distinct reduction peaks due to iron oxide species were observed for FC1, indicating the formation of a complete solid solution of iron–cerium oxide. Further increases in the iron content clearly resulted in reduction peaks at about 375 and 488 °C, which can be attributed to the reduction of iron species, i.e., $Fe_2O_3 \rightarrow Fe_3O_4$ and $Fe_3O_4 \rightarrow Fe^0$ [40,42]. This result demonstrated that the presence and quantity of iron in ceria determines the reducibility of the ceria. The reduction of ceria at low temperatures is suitable for catalyzing redox chemical reactions. It should also be noted that the intensity of the reduction peaks increased with increasing iron content. From the TPR profiles, it was observed that finely dispersed Fe–O was present in FC2 and FC3, which could not be detected by XRD and the other techniques mentioned above.

In order to understand the nature of the interaction between the two metal oxide species, the calcined Ce–Fe–O samples were investigated using the XPS technique (Fig. 5). The XPS spectra of the 3d core level of the samples showed eight peaks corresponding to the three pairs of spin–orbit doublets of CeO_2 [41] and two peaks corresponding to Ce_2O_3. For each doublet, $3d_{5/2}$ corresponds to the label v and $3d_{3/2}$ to u. The details of the origin of each doublet have been reported elsewhere [43]. In Fig. 5a, the peaks labeled v/u, v″/u″, and v‴/u‴ can be assigned to Ce^{4+} and v′/u′ to Ce^{3+} [44]. The two main bands of $Ce3d_{5/2}$, at 883 eV (v) and 885.6 eV (v′), can be ascribed to Ce^{4+} and Ce^{3+}, respectively. However, X-ray diffraction lines corresponding to Ce_2O_3 were not observed. The XRD data

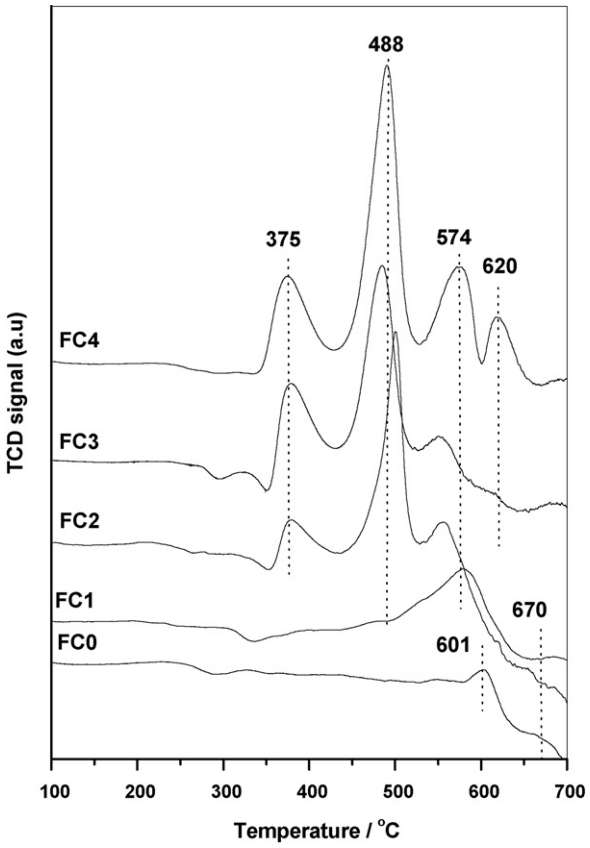

Fig. 4. TPR profiles of the calcined Fe–CeO_2 catalysts as a function of iron content.

revealed the presence of peaks corresponding to CeO_2 in all the samples. Hence, the presence of Ce^{3+} ions can be mainly attributed to the removal of surface hydroxyl groups and oxygen from the CeO_2 surface during exposure of the samples to the X-ray in an ultrahigh vacuum chamber under mild reduction conditions [45]. The photoelectron peaks of O 1s are shown in Fig. 5b. The shape and corresponding binding energies of the XPS peaks were found to be sensitive to composition and surface coverage. The O 1s peak is generally broad and complicated due to the overlapping contributions of oxygen from ceria and iron oxide. The binding energy of the main intense peak at 530.14 in Fe–CeO_2 was the same for the FC1 and FC2 samples; however, with increasing iron content the values shifted to a higher binding energy. The main peak observed at about 530.14 eV arises mainly due to the oxygen atoms that are bound to Ce, judging from the differences in electronegativity [46,47]. The O 1s profiles of the samples were asymmetric and intense, at least for the initial loading of iron; shoulder peaks were also visible for all the samples at higher binding energies (ca. 532.6 eV), indicating the different nature of the bonding of oxygen with Ce and Fe ions. The shoulder peak at 532.6 eV may also be attributed to impurities such as OH^- and CO_2^{3-} species between the oxygen species that are associated with Fe and Ce; however, a difference in the binding energies of the oxygen species with different metal ions cannot be ruled out, an issue that is difficult to resolve. Considerable differences were observed in the BE of the O 1s peak in samples of differing composition. Photoemission spectra from the Fe 2p core level exhibited main line and satellite peaks for both spin–orbit doublets. The main photoemission peak from $2p_{3/2}$ was observed at 710.4 eV for all the samples (Fig. 5c), and a clear satellite, due to the predominant Fe^{3+}, was observed for FC3 and FC4 [48]. The Fe $2p_{1/2}$ main peak was observed at about 725.8 eV. The surface Fe/Ce molar ratios according to the XPS data were 0.257, 0.336, 0.428 and 0.438 for FC1, FC2, FC3 and FC4, respectively. However, monolayer formation was stated in case of 5% Fe/CeO_2 based on the appearance of surface reduction peaks (due to Fe_2O_3), which are absent for FC1 (Fig. 4). The Fe 2p photoemission spectra of the

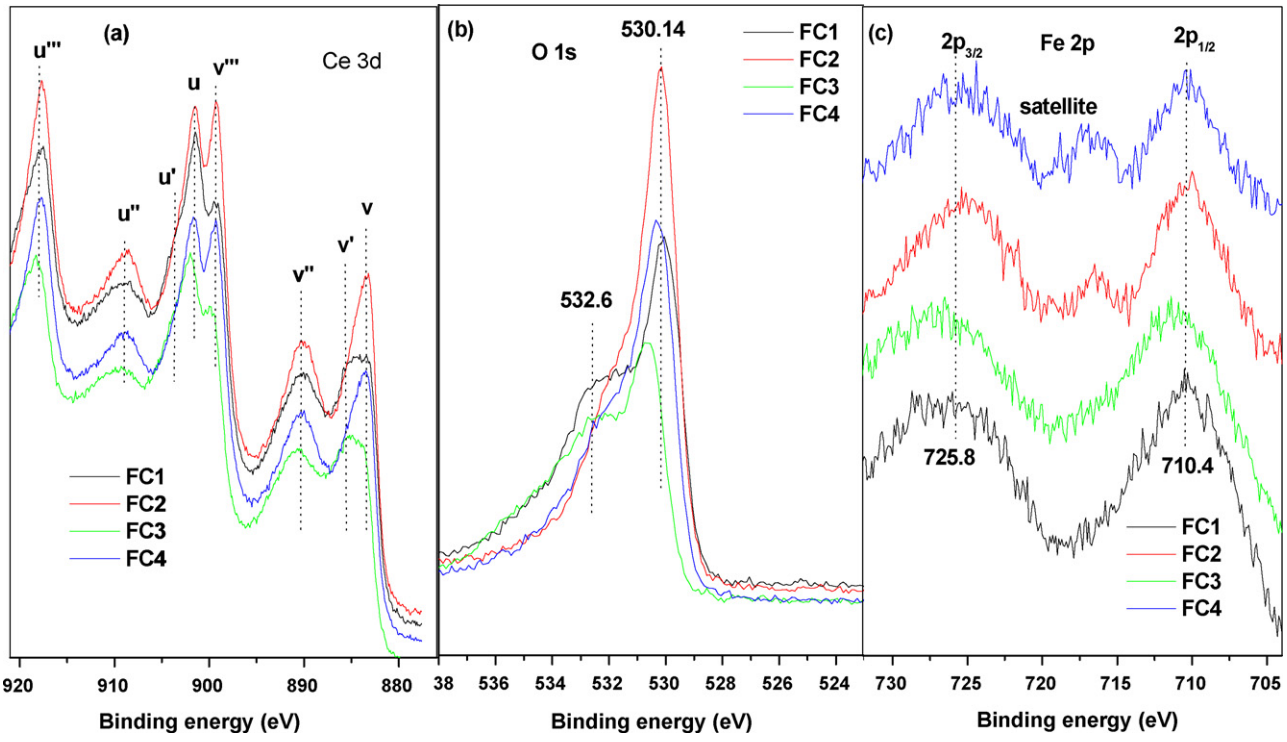

Fig. 5. Photoemission spectra of the freshly calcined Fe–CeO_2 catalysts: (a) Ce 3d, (b) O 1s, (c) Fe 2p.

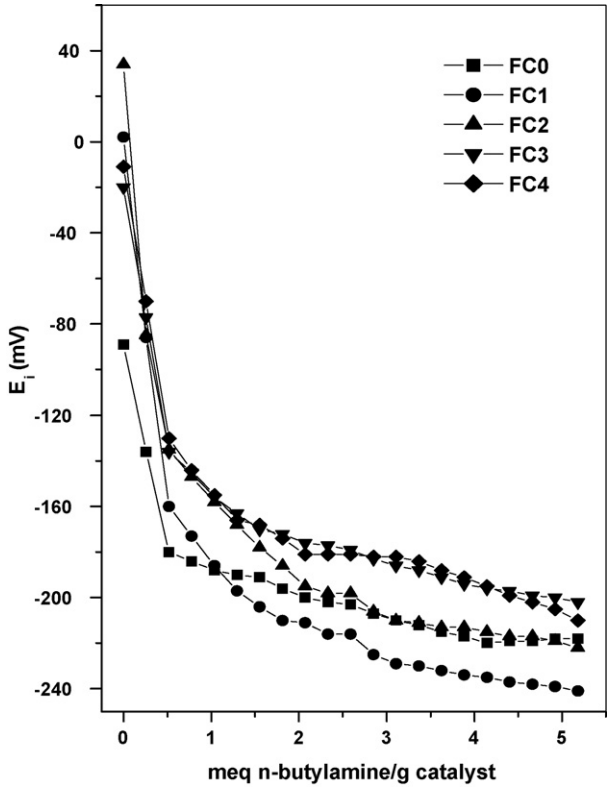

Fig. 6. Potentiometric titration curves of the Fe–CeO_2 catalysts.

FC2 catalyst indicated the presence of finely dispersed iron oxide species.

Acidity measurements for the Fe–Ce–O samples were performed using the potentiometric titration method with *n*-butylamine for colored samples, as described previously [28,29,48]; these acidity measurements enable us to estimate the number of acidic sites and their acidic strength. As a criterion to interpret the obtained results, it was suggested that the initial electrode potential (E_i) be taken to indicate the maximum acid strength of the sites and the value of mequiv.amine/g solid where the plateau is reached to indicate the total number of acidic sites. Nevertheless, the end point of the titration given by the inflexion point of the curve is a good measure to use to compare the acidity of the different samples. Alternatively, the acidic strength of the sites may be classified according to the following scale: $E_i > 100$ mV (very strong sites), $0 < E_i < 100$ mV (strong sites), $100 < E_i < 0$ mV (weak sites), and $E_i < -100$ mV (very weak sites) [49]. The titration curves of the catalysts are shown in Fig. 6. According to the above classification, the samples predominantly exhibited weak and very weak acidic sites, with E_i values in the range of 0 to −230 mV. The total acidity (mmol *t*-butylamine/m^{-2}) and acidic strength (initial electrode potential) as determined by potentiometric titration increased with increasing Fe content up to 5% (FC2), then decreased with further increases in Fe content with the initial addition of *n*-butylamine. The acidity decreases in the order: $5\%Fe/CeO_2 > 2\%Fe/CeO_2 > 20\%Fe/CeO_2 > 10\%Fe/CeO_2 > CeO_2$, which is in accordance with the catalytic activity. Acidity of the catalyst influences the hydrolysis of cyclohexene epoxide into 1,2-cyclohexenediol. The same trend was observed in the acidic strength of the catalysts, probably as a result of the generation of new acidic sites due to interaction of Fe with CeO_2. When the dispersion of Fe was highest in the FC2 sample, supported also by the TPR results (at the theoretical monolayer coverage), both the acidity and the acidic strength were found to be at a maximum.

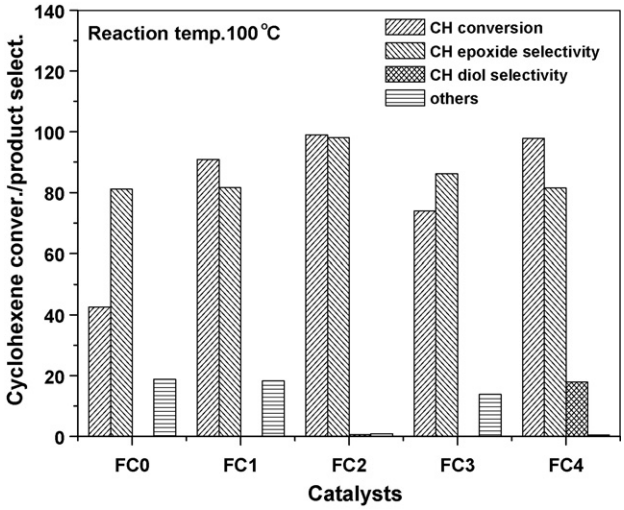

Fig. 7. Effect of catalyst composition on cyclohexene oxidation (reaction conditions: 100 °C, 8 h, 0.1 g catalyst, 10 ml solvent (*t*-butanol), 10 mmol substrate, 10 mmol H_2O_2, 30% aqueous solution).

Moreover, samples with a higher Fe content (above surface saturation coverage) exhibited a loss of acidity and acidic strength, which is probably due to the agglomeration of crystalline Fe_2O_3 on the surface.

3.2. Catalytic activity

Fig. 7 shows the catalytic activity of the different iron–ceria catalysts for cyclohexene oxidation at 100 °C and 1 atm using aqueous hydrogen peroxide (30%) as the oxidizing agent. The screening of the catalysts was carried out under identical conditions. Cyclohexene oxidation yielded mainly cyclohexene oxide (epoxide) and cyclohexane diols, plus cyclohexenol, cyclohexenone, cyclohexanol and cyclohexanone (termed 'others' hereafter) in minor quantities. Cyclohexene conversion and epoxide selectivity varied significantly with catalyst composition. Low cyclohexene conversion ~42% and epoxide selectivity ~82 mol% were observed in the case of pure CeO_2 (FC0), while the others represented about 18 mol%, after 8 h of reaction using *t*-butanol as the solvent. The presence of Fe in the ceria matrix significantly increased the cyclohexene conversion rate and the epoxide selectivity, and the highest cyclohexene conversion (~99 mol%) and epoxide selectivity (98%) rates were observed when FC2 was employed as the catalyst; a small amount of others (<2%) was also produced. Further increases in the Fe content resulted in a decrease in the cyclohexene conversion rate (74 mol%) and epoxide selectivity (84 mol%) for FC3, a cyclohexene conversion comparable with that of FC2 was observed for FC4, epoxide selectivity was lower (82 mol%), with a concomitant increase in diol formation (18 mol%). Fig. 8 shows the catalytic activity of the different Fe–Ce–O catalysts at a reaction temperature of 120 °C. This increase in the reaction temperature increased cyclohexene conversion for the FC0 catalyst, and the formation of diols also increased. The highest cyclohexene conversion (~100 mol%) and epoxide (60%) and diol (38%) selectivities were observed with FC2, but formation of diols was predominant in this case. The use of catalysts with higher Fe contents (FC3 and FC4) resulted in comparable cyclohexene conversion rates, but were lower than that of FC2, with epoxide and diols formed as the major products. Leaching of Fe from the catalysts under the reaction conditions (≤120 °C) was not observed and reused catalyst showed not more than 10% decrease in the conversion or selectivity indicating homogeneous catalysis was absent. It is known that Fe ions can be easily leached in presence of H_2O_2

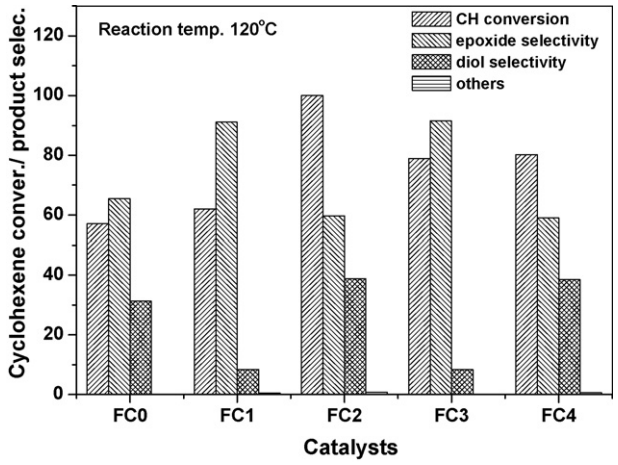

Fig. 8. Effect of catalyst composition on cyclohexene oxidation (reaction conditions: 100 °C, 8 h, 0.1 g catalyst, 10 ml solvent (*t*-butanol), 10 mmol substrate, 10 mmol H_2O_2, 30% aqueous solution).

and polar reagents (diols in this case). The influence of the aprotic/protic nature and polarity of different solvents on the catalytic performance of the FC2 catalyst in the oxidation of cyclohexene on cyclohexene conversion and product selectivity is shown in Fig. 9. These results clearly reveal low cyclohexene conversion rates with acetonitrile and ethylacetate as compared with using *t*-butanol as the solvent, and low epoxide selectivities and the formation of other products were also predominant with acetonitrile and ethylacetate solvents. The aprotic solvent *t*-butanol favored cyclohexene conversion resulting in the formation of the epoxide, while the polar aprotic solvents acetonitrile and ethyl acetate were not selective for epoxide formation and resulted in low conversion rates; the latter two solvents also favored the formation of greater amounts of other products. Hence, all of the reactions were carried out using *t*-butanol as the solvent at different temperatures. The control experiment, in which no catalyst was employed and *t*-butanol was used as the solvent at 100 °C, resulted in a ~40 mol% cyclohexene conversion and ~89 and ~11 mol% selectivity for epoxide and diols, respectively. Decomposition of H_2O_2 over the FC2 catalyst at 100 °C in the absence of substrate molecules under identical conditions showed about 80% and complete decomposition at ≥120 °C.

These catalytic studies of cyclohexene oxidation over various Fe/CeO_2 catalysts showed that an optimum concentration of Fe is required in order to achieve a high epoxide selectivity and that the

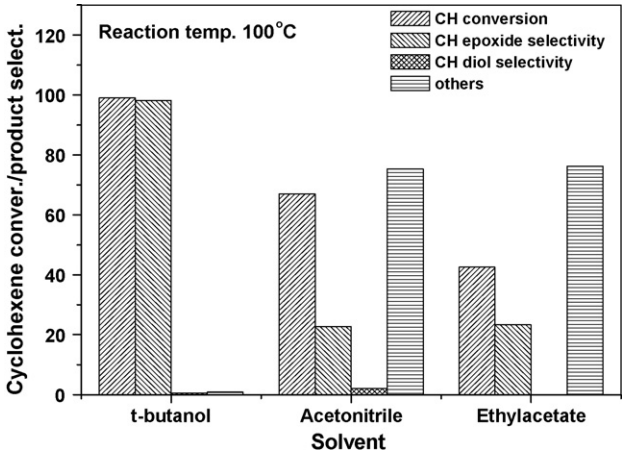

Fig. 9. Effect solvent on cyclohexene oxidation (reaction conditions: 100 °C, 8 h, 0.1 g catalyst, 10 ml solvent, 10 mmol substrate, 10 mmol 30% H_2O_2 aqueous solution).

FC2 catalyst exhibited superior activity and selectivity as compared with the other catalysts investigated.

The activity and epoxide selectivity obtained when employing these catalysts may be explained by referring to the acidity and reducibility measurements and structural properties. Metal oxides are known for their acid–base properties, and their respective strengths and acidity depend on their composition [50]. The potentiometric titration method was used to measure the number of acidic sites and their strength, and the TPR results revealed that the redox properties of the Fe/CeO_2 catalysts are correlated with catalytic activity in cyclohexene oxidation. All of the samples predominantly exhibited weak and very weak acidic sites; however, the FC2 catalyst showed some strong acidic sites with an E_i of about 40 mV (Fig. 6). Hence, the conversion rate of cyclohexene was highest when this catalyst was employed, and the epoxide selectivity also reached a maximum. In addition, as the solvent polarity decreased, the epoxide selectivity also decreased dramatically. Although there were relatively more acidic sites on the catalysts with higher Fe contents (i.e., FC3 and FC4), the catalytic activity and epoxide selectivity were found to be lower in comparison than those of the catalysts with lower Fe contents (FC1 and FC2). This may be attributed to the aggregation of Fe_2O_3 beyond the monolayer coverage on the surface ($x > 5\%$). It has been reported that weak acidic sites, or in other words, a catalyst of greater basicity, may be favorable for the formation of cyclohexenol and cyclohexanone [51]. The TPR results also corroborate the maximum dispersion results of Fe oxide on FC2 in that two reduction peaks due to iron oxide were observed at about 375 and 488 °C. Therefore, it can be inferred that the enhanced redox behavior of the Fe-doped ceria with higher dispersion on FC2 exhibited better catalytic activity. However, the Raman spectra of the FC2 sample did not show any peaks corresponding to iron oxide species, the Fe 2p photoemission spectra of the FC2 catalyst indicated the presence of finely dispersed iron oxide species, and the spectra of the catalysts with high Fe contents (i.e., FC3 and FC4) showed clear satellite peaks corresponding to Fe^{3+}.

4. Conclusions

The activities of a series of catalysts with varying concentrations of iron on ceria were investigated in this study for cyclohexene oxidation. The catalyst with finely dispersed iron oxide on ceria was found to be more active in terms of cyclohexene conversion and more selective towards epoxide formation. The strong and weak acidic sites on the FC2 catalyst were believed to be responsible for the higher cyclohexene conversion rate, and the improved activity was also attributed to the low reduction temperature of the FC2 catalyst with enhanced redox properties. The reducibility of oxides with good lattice oxide transfer to the reactants in the case of the FC2 catalyst proved to be effective and selective towards the oxidized product.

Acknowledgement

The authors thank the National Science Council, Taiwan, for the research grant (97-2628-M-194-002).

References

[1] B.J. Cooper, W.D.J. Evans, B. Harrison, A. Crucq, A. Frennet, Catalysis and Automotive Pollution Control. I, Elsevier, Amsterdam, 1987, pp. 117–219.
[2] T. Bunluesin, R.J. Gorte, Appl. Catal. B 15 (1998) 107–114.
[3] T. Shido, Y. Iwasawa, J. Catal. 141 (1993) 71–81.
[4] Y. Zhang, S. Anderson, M. Muhammed, Appl. Catal. B 6 (1995) 325–327.
[5] P. Vidmar, P. Fornasiero, J. Kaspar, G. Gubitosa, M. Graziani, J. Catal. 171 (1997) 160–168.
[6] L. Ilieva, G. Pantaleo, I. Ivanov, R. Nedyalkova, A.M. Venezia, D. Andreeva, Catal. Today 139 (2008) 168–173.

[7] A. Ozaki, K. Aika, in: J.R. Anderson, M. Boudart (Eds.), Catalysis, Science and Technology, vol. 1, Springer-Verlag, Berlin, 1981 (ch. 3).
[8] U. Schwertmann, R.M. Cornell, The Iron Oxides: Structure, Properties, Reactions, Occurrences and Uses, Wiley–VCH, New York, 2003.
[9] F.J. Perez-Alonso, M.L. Granados, M. Ojeda, P. Terreros, S. Rojas, Chem. Mater. 17 (2005) 2329–2339.
[10] S.V. Manorama, N. Izu, W. Shin, I. Matsubara, N. Murayama, Sen. Actuators B 89 (2003) 299–304.
[11] Y. Kamimura, S. Sato, R. Takahashi, T. Sodesawa, T. Akashi, Appl. Catal. A 252 (2003) 399–410.
[12] G. Neri, A. Bonavita, G. Rizzo, S. Galvagno, S. Capone, P. Siciliano, Sens. Actuators B 111–112 (2005) 78–83.
[13] J. Gaube, H.F. Klein, Appl. Catal. A 350 (2008) 126–132.
[14] B. Horvath, M. Hronec, Appl. Catal. A 347 (2008) 72–80.
[15] S. Ted Oyama, Mechanisms in Homogeneous and Heterogeneous Epoxidation Catalysis, Elsevier, Netherlands, 2008.
[16] J.M. Thomas, R. Raja, Aust. J. Chem. 54 (2001) 551–560.
[17] M.N. Timofeeva, O.A. Kholdeeva, S.H. Jhung, J.S. Chang, Appl. Catal. A 345 (2008) 195–200.
[18] R. Luque, S.K. Badamali, J.H. Clark, M. Fleming, D.J. Macquarrie, Appl. Catal. A 341 (2008) 154–159.
[19] S. Mukerjee, S. Samanta, A. Bhaumik, B.C. Ray, Appl. Catal. B 68 (2006) 12–20.
[20] S. Bin, C. Junru, H. Jiayuan, L. Xianjun, J. Inorg. Biochem. 100 (2006) 1308–1313.
[21] E.M. Serwicka, J. Poltowicz, K. Bahranowski, Z. Olejniczak, W. Jones, Appl. Catal. A 275 (2004) 9–14.
[22] B.G. Choi, R. Song, W. Nam, B. Jeong, Chem. Commun. 23 (2005) 2960–2962.
[23] O.A. Kholdeeva, T.A. Trubitsina, M.N. Timofeeva, G.M. Maksimov, R.I. Maksimovskaya, V.A. Rogov, J. Mol. Catal. A 232 (2005) 173–178.
[24] F. Farzaneh, S. Sadeghi, L. Turkian, M. Ghandi, J. Mol. Catal. A 132 (1998) 255–261.
[25] S.H. Lau, V. Caps, K.W. Yeung, K.Y. Wong, S.C. Tsang, Micropor. Mesopor. Mater. 32 (1999) 279–285.
[26] G. Grigoropoulou, J.H. Clark, J.A. Elings, Green Chem. 5 (2003) 1–7.
[27] R. Noyori, M. Aoki, K. Sato, Chem. Commun. 16 (2003) 1977–1986.
[28] K. Narasimha Rao, K. Mohan Reddy, N. Lingaiah, I. Suryanarayana, P.S. Sai Prasad, Appl. Catal. A 300 (2006) 139–146.
[29] L.R. Pizzio, P.G. Vazquez, C.V. Caceres, M.N. Blanco, Appl. Catal. A 256 (2003) 125–139.
[30] S. Tsunekawa, T. Fukuda, A. Kasuya, J. Appl. Phys. 87 (2000) 1318–1321.
[31] H.H. Tippins, Phys. Rev. B 1 (1970) 126–135.
[32] M. Schwidder, M.S. Kumar, K. Klementiev, M.M. Pohl, A. Brückner, W. Grünert, J. Catal. 231 (2005) 314–330.
[33] G.D. Pirngruber, P.K. Roy, R. Prins, Phys. Chem. Chem. Phys. 8 (2006) 3939–3950.
[34] M.S. Kumar, M. Schwidder, W. Grünert, A. Brückner, J. Catal. 227 (2004) 384–397.
[35] J. Torrent, V. Barrón, Clays Clay Miner. 51 (2003) 309–317.
[36] L. Lu, L. Li, X. Wang, G. Li, J. Phys. Chem. B 109 (2005) 17151–17156.
[37] K. Nakamoto, Infrared and Raman Spectra of Inorganic and Coordination Compounds, John Wiley and Sons, 1978, p. 108.
[38] W.H. Weber, K.C. Hass, J.R. McBride, Phys. Rev. B 48 (1993) 178–186.
[39] K. Sun, H. Xia, Z. Feng, R. van Santen, E. Hensen, Can Li, J. Catal. 254 (2008) 383–396.
[40] G. Neri, A. Pistone, C. Milone, S. Galvagno, Appl. Catal. B 38 (2002) 321–329.
[41] S. Damyanova, J.M.C. Bueno, Appl. Catal. A 253 (2003) 135–150.
[42] K. Li, H. Wang, Y. Wei, M. Liu, J. Rare Earths 26 (2008) 245–249.
[43] B.M. Reddy, A. Khan, Y. Yamada, T. Kobayashi, S. Loridant, J.C. Volta, J. Phys. Chem. B 107 (2003) 5162–5167.
[44] A. Galtayries, R. Sporken, J. Riga, G. Blanchard, R. Caudano, J. Electron Spectrosc. Relat. Phenom. 88–91 (1998) 951–956.
[45] S. Damyanova, C.A. Perez, M. Schmal, J.M.C. Bueno, Appl. Catal. A 234 (2002) 271–282.
[46] D. Briggs, M.P. Seah, Practical Surface Analysis: Auger and X-Ray Photoelectron Spectroscopy, vol. 1, 2nd ed., Wiley, New York, 1990.
[47] G.A. Sawatzky, D. Post, Phys. Rev. B 20 (1979) 1546–1555.
[48] T. Mathew, N.R. Shiju, K. Sreekumar, B.S. Rao, C.S. Gopinath, J. Catal. 210 (2002) 405–417.
[49] C.I.D. Ruby, G. Pecchi, Appl. Catal. 14 (1985) 15–21.
[50] R. Zavoianu, R. Birjega, O. Dumitru Pavel, A. Cruceanu, M. Alifanti, Appl. Catal. A 286 (2005) 211–220.
[51] W. Fan, P. Wu, T. Tatsumi, J. Catal. 256 (2008) 62–73.